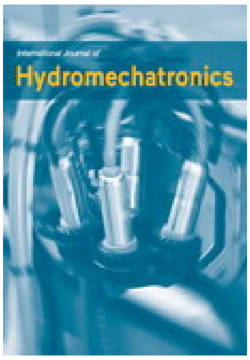

International Journal of Hydromechatronics

ISSN online: 2515-0472 - ISSN print: 2515-0464
https://www.inderscience.com/ijhm

Automation and synchronisation on electro-hydraulic lifting system of tunnel boring machine segment assembly

Xuyang Chen, Yang Tang, Xin Huang, Wujun Wang, Junke Guo, Fulong Lin, Lianhui Jia, Huayong Yang, Yi Zhu

DOI: 10.1504/IJHM.2024.10068376

Article History:

Received:	28 August 2024
Last revised:	08 October 2024
Accepted:	22 October 2024
Published online:	13 March 2025

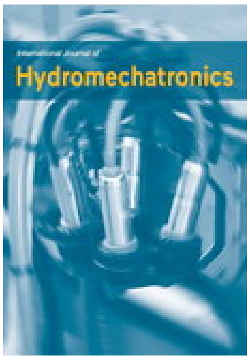

International Journal of Hydromechatronics

ISSN online: 2515-0472 - ISSN print: 2515-0464
https://www.inderscience.com/ijhm

Automation and synchronisation on electro-hydraulic lifting system of tunnel boring machine segment assembly

Xuyang Chen, Yang Tang, Xin Huang, Wujun Wang, Junke Guo, Fulong Lin, Lianhui Jia, Huayong Yang, Yi Zhu

DOI: 10.1504/IJHM.2024.10068376

Article History:

Received:	28 August 2024
Last revised:	08 October 2024
Accepted:	22 October 2024
Published online:	12 March 2025

Automation and synchronisation on electro-hydraulic lifting system of tunnel boring machine segment assembly

Xuyang Chen, Yang Tang and Xin Huang

State Key Laboratory of Fluid Power Components
and Mechatronic Systems,
Zhejiang University,
310027 Hangzhou, China
Email: 352206277@qq.com
Email: 1206120664@qq.com
Email: 22260027@zju.edu.cn

Wujun Wang

Department of Energy Technology,
KTH Royal Institute of Technology,
10044, Stockholm, Sweden
Email: wujun.wang@energy.kth.se

Junke Guo, Fulong Lin and Lianhui Jia

Electrical Research Institute of China Railway,
Engineering Equipment Group Co., Ltd
450047 Zhengzhou, China
Email: 1217478594@qq.com
Email: 2312763391@qq.com
Email: gjkzzu@163.com

Huayong Yang

State Key Laboratory of Fluid Power Components
and Mechatronic Systems,
Zhejiang University,
310027 Hangzhou, China
Email: yhy@zju.edu.cn

Yi Zhu*

State Key Laboratory of Fluid Power Components
and Mechatronic Systems,
Zhejiang University,
310027 Hangzhou, China
and
Ningbo Innovation Centre,
Zhejiang University,
Ningbo 315100, China
Email: yiz@zju.edu.cn
*Corresponding author

Abstract: Segment lifting, performed by an electro-hydraulic system including two cylinders, is a crucial step in segment grasping, transporting, and assembly in tunnel boring machines. Due to heavy and uneven loading, large vibration, uncertainty of parameters, and nonlinear friction, it is difficult to develop an accurate physical model. This paper presents a comprehensive procedure to achieve two-cylinder automation and synchronisation according to the actual engineering requirements and environments. An improved deviation compensation recursive least squares identification algorithm with a forgetting factor was used to identify the key parameters of the model. To achieve synchronous control and precise control of the lifting system, SMC with improved sliding mode approach rate and the deviation coupling method of fusion single neuron PID were designed and verified by simulation. A full-scale bench test was also performed to show that the tracking steady-state error is below 4 mm, and the synchronisation error is below 2 mm.

Keywords: tunnel boring; segment assembly; parameter identification; synchronous control; automation.

Reference to this paper should be made as follows: Chen, X., Tang, Y., Huang, X., Wang, W., Guo, J., Lin, F., Jia, L., Yang, H. and Zhu, Y. (2025) ‘Automation and synchronisation on electro-hydraulic lifting system of tunnel boring machine segment assembly’, *Int. J. Hydromechatronics*, Vol. 8, No. 1, pp.94–120.

Biographical notes: Xuyang Chen received his BS degree in Software Engineering from North University of China, Taiyuan, China, in 2015, and MS degree in Mechanical Engineering from Taiyuan University of Technology, Taiyuan, China, in 2018, and PhD degree in Mechatronics Engineering with School of Mechanical Engineering, Zhejiang University, Hangzhou, China, in 2024. His research areas include intelligent manufacturing and robotics, fault diagnosis. He is mainly engaged in machine vision, electromechanical hydraulic control and signal processing research.

Yang Tang received his BS degree in 2022 from Zhejiang University, Zhejiang, China. He is currently pursuing a Doctoral degree at the School of Mechanical Engineering, Zhejiang University, where his research focuses on the lightweight and modular design of electro-hydraulic actuation systems.

Xin Huang received his BS degree from Wuhan University of Technology, Wuhan, China in 2022. He is currently pursuing a Masters degree at the School of Engineering at Zhejiang University.

Wujun Wang received his BSc degree in Mechanical Engineering at Xi'dian University in 2007, MSc degree in Engineering Thermophysics at Zhejiang University in 2010 in China, and received PhD degree in Department of Energy Technolog at KTH Royal Institute of Technology in 2015 in Sweden. He is currently a researcher at the Heat and Power Division of the Energy Department within the Energy Department. His specific research topics include high-temperature heat transfer phenomenon, hybrid solar-Brayton cycle, jet impingement, optical ray tracing, high-temperature structure materials and coatings.

Junke Guo received his BS degree and MS degree in Mechanical and Electronic Engineering from Zhengzhou University, Zhengzhou, China, in 2015 and 2018. He is currently an Electrical Designer and Intermediate Engineer at China Railway Engineering Equipment Group Co., Ltd.

Fulong Lin received his BS degree and MS degree in Mechanical Engineering from Shijiazhuang Tiedao University, Shijiazhuang, China, in 2009 and 2016. He is currently the Head and Senior Engineer of the Electrical Research Institute of China Railway Engineering Equipment Group Co., Ltd.

Lianhui Jia received his BS degree from Hebei University of Engineering, Handan, China, in 2004, and MS degree in Mechanical Engineering from Shijiazhuang Tiedao University, Shijiazhuang, China, in 2016. He is currently the Chief Engineer and Professor level Senior Engineer of China Railway Engineering Equipment Group Co., Ltd.

Huayong Yang received his PhD degree in Fluid Power Transmission and Control from the University of Bath, Bath, UK, in 1988. He is currently the Director with the State Key Laboratory of Fluid Power and Mechatronic Systems, Zhejiang University, Hangzhou, China. He also serves as an Academician with the China Engineering Academy.

Yi Zhu received his PhD degree in Machine Design from the KTH Royal Institute of Technology, Stockholm, Sweden, in 2013. He is currently an Associate Professor with the State Key Laboratory of Fluid Power and Mechatronic Systems, Zhejiang University, Hangzhou, China. His main research includes tribology of additive manufacturing and novel additive manufacturing design in hydraulic components. He is an Associate Editor for the *ASME Journal of Tribology* and a Guest Editor for Additive Manufacturing Automation.

1 Introduction

During tunnel boring machine (TBM) operation, segment assembly is a key factor affecting boring speed, quality, and safety. Current TBM segment assembly still relies on manual operation and technician experience. Segment assembly automation is a trend to improve efficiency and safety (Chen et al., 2023). In automatic segment assembly, there are three main segment motions including translating, rotating, and lifting, driven by electro-hydraulic systems, as shown in Figure 1. Lifting segment is achieved by the synchronous motion of two hydraulic cylinders. However, various factors negatively affect the synchronous motion and assembly accuracy (Yuan et al., 2020), such as a large inertia force (each segment weighted more than 2 tons), a long cylinder distance (1.2 m), uneven loads, oil leakage, nonlinear friction resistance, large manufacturing and assemble deviations. Therefore, it is essential to develop an automatic lifting system to achieve two-cylinder synchronisation and segment position control.

Common synchronous control strategies include master-slave control (Han et al., 2018), parallel control (Wang et al., 2022), cross-coupling control (Hao et al., 2020), and deviation-coupling control. Parallel and master-slave synchronous control have simple controller structures but relatively low anti-interference capability. Master-slave control controls and adjusts a hydraulic synchronous subsystem according to the error between its own and the ideal subsystem output. However, the assembly machine lifting system has a complex structure and is affected by nonlinear factors resulting in a large error in each subsystem. Parallel control drives multiple actuators simultaneously through independent hydraulic circuits. The synchronisation is negatively influenced when the difference between the subsystems is large. Cross-coupling synchronous control and deviation-coupling synchronous control also consider their motion states and the two adjacent channels, which cannot meet the accuracy requirements.

Research has been conducted on combining intelligent control algorithms with synchronous control strategies to improve control accuracy. Intelligent control algorithms, such as sliding mode control (SMC) (Guo et al., 2022; Li et al., 2022; Kuang et al., 2021; Li et al., 2022), anti-disturbance control (Qi et al., 2022; Ma et al., 2023; Chen and Hu, 2022), model predictive control (Liu et al., 2022), robust control (Shi et al., 2023; Sun and Yuan, 2021; Wu et al., 2022), fuzzy PID control (Hu and Zhang, 2022; Yuan and Zhao, 2022), adaptive control (Guo et al., 2021; Wang et al., 2022), and backstepping control (Wu et al., 2022), are widely used. However, these control algorithms often have a high computational complexity, a relatively large cumulative error, and is easy to lose control due to a system failure. An engineering application, such as a TBM segment assembly, needs to consider economy, efficiency, and robustness. Moreover, accurate system physical parameters and harsh system environments (such as oil leakage, nonlinear friction, vibration, etc.) further impede these algorithms to being used in the system (Yang et al., 2010; Liu et al., 2019; Li and Cao, 2021). Because many parameters cannot be measured or calculated due to the large number and the complexity of physical parameters in high-order hydraulic systems. Some researchers use disturbance compensation methods to reduce errors, such as feedforward compensation (Yabui and Inoue, 2019; Li et al., 2020) and disturbance observers. However, these works do not consider the disturbance resistance, stability, synchronisation, and accuracy of heavy-load, large-delay systems.

This paper aims to achieve automation for the electro-hydraulic lifting system in TBM segment assembly. The system should have a maximum synchronisation error below 2 mm with a heavy load (maximum load 4t) and uneven load and a large stroke (up to 1.2 m). A signal preprocessing method was first designed to reduce system noise. An improved deviation compensation recursive least squares identification algorithm with a forgetting factor was proposed to identify the key parameters of the model. Moreover, an adaptive feedforward cancellation algorithm and the extended state observer were used to compensate for the disturbance. To achieve synchronous control and precise control of the lifting system, SMC with improved sliding mode approach rate and the deviation coupling method of fusion single neuron PID are designed and verified by simulation while a full-scale bench test was also performed. The results show that the trajectory tracking steady-state error of this method is below 4 mm, and the synchronisation error is below 2 mm.

2 System model

2.1 Description of the system

The system model is based on the lifting system of the 6-metre earth pressure balance shield segment assembly machine in Figure 1(a), which consists of two independent hydraulic cylinders, the left and the lifting right cylinders. A schematic of the lifting electro-hydraulic system is shown in Figure 1(b), which includes hydraulic cylinders, amplifiers, balance valves, and proportional multi-way valves. The schematic diagram of the lifting hydraulic system is shown in Figure 2.

Figure 1 (a) Schematic of a segment assembly machine and (b) the lifting electro-hydraulic system (see online version for colours)

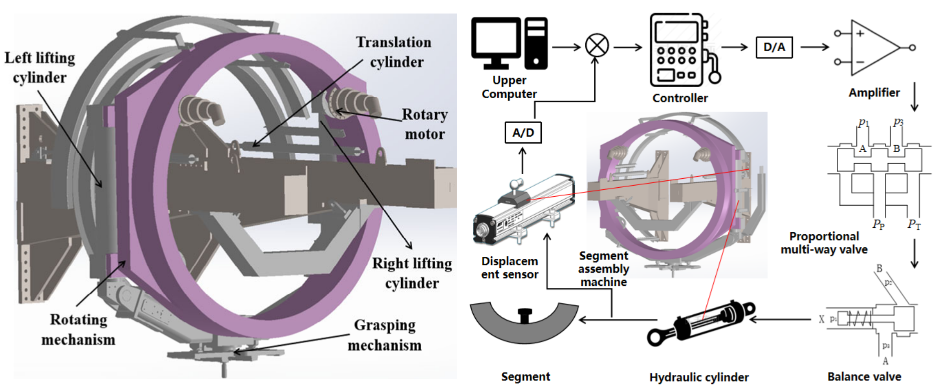

(a) (b)

When the assembly machine moves in translation, the translation cylinder drives the entire assembly machine and the pipe segment to move forward and backward. When the assembly machine moves in rotation, the rotary motor drives the rotary mechanism (except the rotary frame), the lifting mechanism, the grabbing mechanism and the pipe segment to move in rotation. When the assembly machine moves in lifting, the lifting cylinder drives the grabbing mechanism and the pipe segment to move up and down.

Figure 1(b) shows the basic structure of the system, which can be divided into four steps:

1 the computer generates control signals to the controller

2 the voltage control signal is converted by the amplifier into a current signal capable of controlling the multi-way valve

3 the multi-way valve then moves based on the current signal from the control output

4 the hydraulic cylinder expands and contracts according to the signal from the multi-way valve.

In addition, the displacement sensor transmits the displacement signal back to the controller in real-time.

Figure 2 Schematic diagram of lifting hydraulic system for segment assembly machine (see online version for colours)

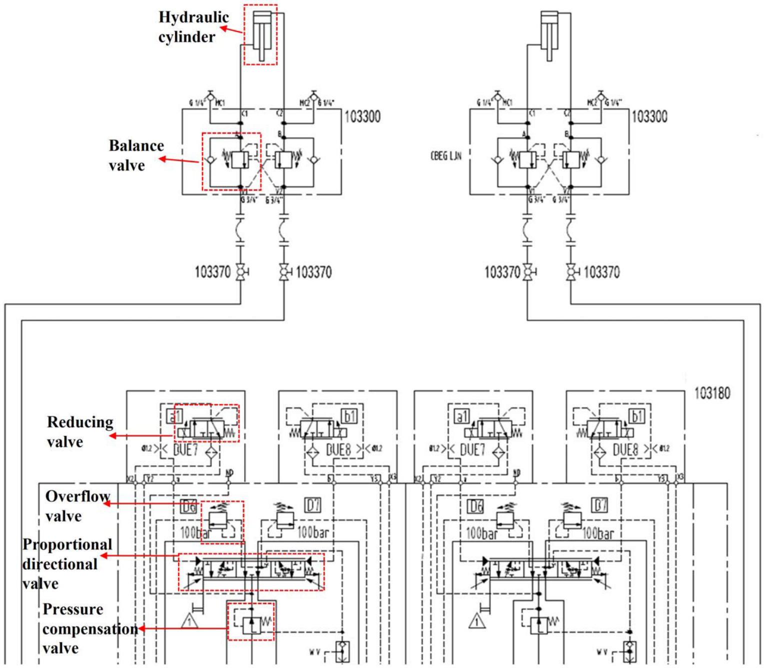

2.2 Electro-hydraulic proportional system model of the lifting mechanism

The flow equation of the multi-way valve is:

$$q_s = K_q I \tag{1}$$

where q_s is the flow rate of the proportional valve, K_q is the flow gain, and I is the input current of the proportional valve.

The continuous flow rate of the hydraulic cylinder is:

$$q_L = C_{tp} p_L + \frac{V_e}{4\beta_e}\frac{dp_L}{dt} + \frac{k+1}{2}A_p\frac{dy}{dt} \tag{2}$$

where q_L is the flow rate of the lifting cylinder, C_{tp} is the total leakage coefficient of the lifting cylinder, p_L is the load pressure of the lifting cylinder, V_e is the effective volume of the lifting cylinder, β_e is the oil volume elastic modulus, A_p is the non-rod chamber area of the lifting cylinder, k is the area ratio between a non-rod chamber and the rod chamber.

The hydraulic cylinder force balance equation is:

$$m\frac{d^2y}{dt^2} + B_p\frac{dy}{dt} + p_2 A_p + F_L = A_0 p_1 \tag{3}$$

where m is half the mass of the segment, B_p is the viscous damping coefficient, p_1 is the rod chamber pressure, p_2 is the non-rod chamber pressure, F_L is the load interference force, A_0 is the rod chamber area, according to the two cavity pressures and the relationship between the action area, equation (3) can be transformed into:

$$m\frac{d^2y}{dt^2}+B_p\frac{dy}{dt}+F_S-A_pp_L=0 \tag{4}$$

where $F_S = F_L + (1-k)A_pp_s$, and p is the oil pressure.

Considering equations (1)–(4) and performing the Laplace transformation, the mathematical model of a single proportional valve-controlled hydraulic cylinder is obtained:

$$Y(s)=\frac{K_qI-\frac{C_{tp}F_S}{A_p}\left(\frac{V_e}{4C_{tp}\beta_e}s+1\right)}{s\left[\frac{mV_e}{4\beta_eA_p}s^2+\left(\frac{mC_{tp}}{4A_p}+\frac{V_eB_p}{4A_p\beta_e}\right)s+\left(\frac{B_pC_{tp}}{A_p}+\frac{A_p(k+1)}{2}\right)\right]} \tag{5}$$

where s is the Laplace transform factor. Neglecting the viscous damping of oil, it can be simplified to:

$$Y(s)=\frac{\frac{K_qI}{(k+1)A_p}-\frac{2C_{tp}F_S}{(k+1)A_p^2}\left(\frac{V_e}{4C_{tp}\beta_e}s+1\right)}{s\left(\frac{s^2}{\omega_h^2}+\frac{2\xi s}{\omega_h}+1\right)} \tag{6}$$

where ξ is the system damping coefficient,   is the system natural frequency.

Specific values are shown in Table 1.

3 Parameter identification

3.1 Identification signal pre-processing

Since the input signal to be identified is the output signal of the sensor, there are often various interferences, measurement errors, and other noises in the experiment, which directly lead to inaccurate identification models. Particularly, vibration noise is quite high in the lifting system due to the heavy load, large hysteresis, and large friction disturbance. Therefore, signal pre-processing is an indispensable step for parameter identification. Figure 3 is the flow chart of the signal pre-processing method used in this article.

The basic steps of signal processing are as follows:

1 The cylinder displacement signal obtained by the test bench is first decomposed by TVF-EMD, where the number of components K is set to 5. If the setting is too large, the bandwidth of each IMF component obtained by decomposition is too narrow and cannot contain enough fault-related information; if the parameter setting is too small, the IMF component bandwidth is too wide and it is easy to introduce too much redundant noise.

2 The component IMF5 containing the useful signal is screened out by the component with the maximum kurtosis value. And the IMF5 component is denoised and smoothed by Kalman filtering and Savitzky-Golay smoothing.

3 The IMF5 component is decomposed by MVMD to further decompose the useful component IMF1. The number of components K is set to 3. Further purification of the signal is achieved and noise is removed.

4 The useful component IMF1 is denoised by Butterworth filtering.

5 The final signal processing result is obtained by MVMD reconstruction. Provide good conditions for the accuracy of subsequent system identification.

Figure 3 Signal pre-processing flow chart

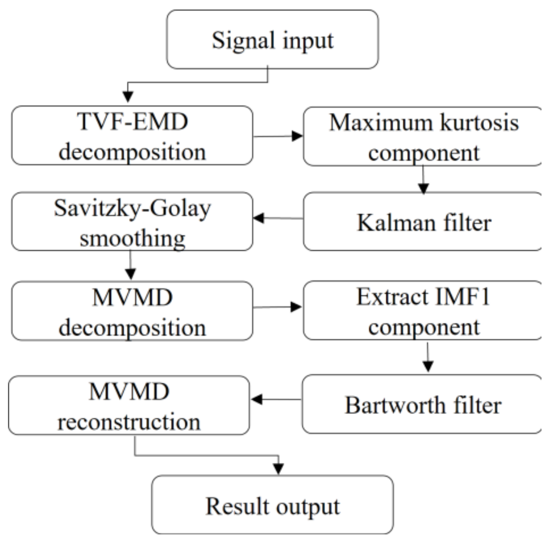

Since the sampling frequency of the assembly machine controller is low and the noise interference is large, time-varying filter empirical mode decomposition (TVF-EMD) is used in filtering. The method obtains the intrinsic mode function (IMF) through time-varying filtering on the given sequence and dividing local high- and low-frequency components based on the transient amplitude and frequency, and adaptive local cutoff frequency, which solves the denoising and signal decomposition problems of low-frequency sampling signals with complex noise to a limited extent.

Moreover, a multivariate variational mode decomposition (MVMD) method is used to improve the frequency separation performance and increase the stability at low sampling rates and robustness. It extends the traditional VMD algorithm from one dimension to multiple dimensions, providing great convenience for processing multi-variable or multi-channel data while ensuring the consistency of component frequencies during multi-channel decomposition. A variational model is introduced in the signal decomposition process. In this process, the IMF component of each channel iteratively updates its centre frequency and bandwidth at the same time, thereby adaptively obtaining k narrowband IMF components.

3.2 Improved bias compensation recursive least squares identification algorithm with forgetting factor

The parameters in the mathematical model are closely related to the structure, operating state, and attitude of the assembly machine. It is difficult or even impossible to obtain all accurate parameters from a complicated system (Kroll and Fischer, 2021; Lin et al., 2022; Zerdali et al., 2021). Therefore, the key parameters in the model are estimated based on the least squares method.

According to the previously developed model, the system model is defined as third-order, and its discrete difference equation is:

$$y(k) + a_1 y(k-1) + a_2 y(k-2) + a_3 y(k-3) = b_1 u(k-1) + d \tag{7}$$

where $y(k)$ and $u(k)$ are the input and output of the system, and d is composite disturbances. The parameter identification of an electro-hydraulic proportional system can be regarded as parameter $[a_1, a_2, a_3, b_1]$ identification.

Written in the least squares form:

$$y(k) = \varphi(k)\theta + e(k) \tag{8}$$

$\varphi(k)$ and θ are defined as:

$$\begin{aligned} \varphi(k) &= [-y(k-1), -y(k-2), -y(k-3)] \\ \theta &= \left[a_1, a_2, a_3, b_1\right] \end{aligned} \tag{9}$$

The estimation error criterion function J of the system parameter vector is:

$$J(k) = J(k-1) + \frac{\left[y(k) - \varphi^T(k)\hat{\theta}(k-1)\right]^2}{\lambda + \varphi^T(k)P(k-1)\varphi(k)} \tag{10}$$

where $I - K(k)\varphi^T(k)$, and λ is the forgetting factor.

The least squares estimate of the system with the forgetting factor is:

$$y(k) - \varphi^T(k)\hat{\theta}(k-1) \tag{11}$$

$$K(k) = \frac{P(k-1)\varphi(k)}{\lambda + \varphi^T(k)P(k-1)\varphi(k)} \tag{12}$$

Through matrix calculation and induction, the bias-compensated recursive least squares estimate with forgetting factor can be obtained:

$$\begin{aligned} \hat{\theta}_c(k) &= \hat{\theta}(k) + k\hat{\sigma}_w^2(k)P(k)D\hat{\theta}_c(k-1) \\ \hat{\sigma}_w^2(k) &= \frac{J(k)}{k[1 + \hat{\theta}_c(k-1)D\hat{\theta}(k)]} \\ D &= \begin{pmatrix} I & 0 \\ 0 & 0 \end{pmatrix} \end{aligned} \tag{13}$$

where $\hat{\sigma}_w^2(k)$ is the estimated value of the unknown disturbance variance.

Since the bias-compensated recursive least squares algorithm is sensitive to outliers, multicollinearity, and nonlinearity, and requires a high sampling number, mean values are used to improve the bias-compensated recursive least squares with forgetting factor, which can be expressed as:

$$\hat{\theta}(k) = \hat{\theta}(k-1) + K(k)\left[mean\left(y(k) - \varphi^T(k)\hat{\theta}(k-1)\right)\right] \tag{14}$$

$$\hat{\theta}_c(k) = \hat{\theta}(k) + mean\left(k\hat{\sigma}_w^2(k)P(k)D\hat{\theta}_c(k-1)\right) \tag{15}$$

4 Control design

According to the structural characteristics of the lifting system of the segment assembly machine, an SMC with an improved sliding mode approach rate and a deviation coupling control strategy integrating single neuron PID were designed for the synchronous control problem of multiple hydraulic cylinders in the lifting system, as shown in Figure 4 (Qian et al., 2023; Li et al., 2019; Ding et al., 2024).

Figure 4 Schematic diagram of control flow

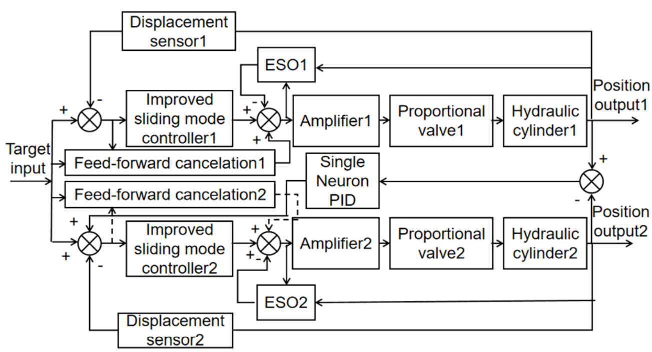

4.1 SMC with improved approach rate

The sliding mode approach rate is used to improve the chattering problem of sliding mode. The transfer function in Section 3 is simplified as the following transfer function:

$$x_p''' + aa_2 x_p'' + aa_1 x_p' + aa_0 x_p = bb_0 u + d \tag{16}$$

$$\begin{cases} x_1 = x_p = y(k) \\ x_2 = x_p' = y(k-1) \\ x_3 = x_p'' = y(k-2) \end{cases} \tag{17}$$

Therefore, the state equation is obtained as:

$$\begin{cases} x_1^{'} = x_2 \\ x_2^{'} = x_3 \\ x_3^{'} = -aa_0 x_1 - aa_1 x_2 - aa_2 x_3 + bb_0 u + d \end{cases} \tag{18}$$

The matrix form is:

$$\begin{bmatrix} x_1^{'} \\ x_2^{'} \\ x_3^{'} \end{bmatrix} = \begin{bmatrix} 0 & 1 & 0 \\ 0 & 0 & 1 \\ -aa_0 & -aa_1 & -aa_2 \end{bmatrix} \begin{bmatrix} x_1 \\ x_2 \\ x_3 \end{bmatrix} + \begin{bmatrix} B_1 \\ B_2 \\ B_3 \end{bmatrix} u \tag{19}$$

$$f(x) = -aa_0 x_1 - aa_1 x_2 - aa_2 x_3 \tag{20}$$

The systematic deviation is:

$$e = r - y \tag{21}$$

The motor output displacement deviation is used as the state variable of the system:

$$\begin{cases} e_1 = e = r - y \\ e_2 = e' = r' - y' \\ e_3 = e'' = r'' - y'' \end{cases} \tag{22}$$

Then the state equation with the system tracking error as a variable can be expressed as:

$$\begin{cases} e_1' = e_2 \\ e_2' = e_3 \\ e_3' = -a_0 e_1 - a_1 e_2 - a_2 e_3 + b_0 u(t) + d \end{cases} \tag{23}$$

Let the system switching function by:

$$s = c_1 e_1 + c_2 e_2 + e_3 \tag{24}$$

where c_1 and c_2 are the sliding mode surface design coefficients. Both are positive numbers, which determine the dynamic quality of the sliding mode.

To prevent chattering, the approach rate is designed, and the tanh function is used instead of the sign function, which is:

$$s' = -k_0 \tanh|s| - k_1 |s|^{\tanh|s|}, k_0 > 0, k_1 > 0 \tag{25}$$

Substituting the switching function, the system error control function can be obtained as:

$$u = \frac{1}{b_0}\left[-a_0 e_1 + (c_1 - a_1) e_2 + (c_2 - a_2) e_3 + d + k_0 \tanh|s| + k_1 |s|^{\tanh|s|}\right] \tag{26}$$

4.2 Stability proof

Define the Lyapunov function as follows:

$$V = \frac{1}{2}s^2 \tag{27}$$

Combining equations (23)–(27) the derivation of equation (28) is as follows:

$$V' = s \cdot s' = s\left[-k_0 \tanh|s| - k_1 |s|^{\tanh|s|}\right] < 0, k_0 > 0, k_1 > 0 \tag{28}$$

4.3 Adaptive feedforward cancellation

Adaptive feedforward cancellation produces an output u, which can compensate for the error e caused by the disturbance d by updating the adaptive parameters p and q. k is the number of samples. The adaptive algorithm of AFC compensates for disturbances by updating adaptive parameters. The output and adaptive algorithm are shown in the following formula (Li et al., 2020):

$$\begin{aligned} u(k) &= p(k-1)\sin(\omega_d Tk) + q(k-1)\cos(\omega_d Tk) \\ p(k) &= p(k-1) + \lambda e(k)\sin(\omega_d Tk + \theta) \\ q(k) &= q(k-1) + \lambda e(k)\cos(\omega_d Tk + \theta) \end{aligned} \tag{29}$$

The interference d is offset by updating the adaptive parameters $p(k)$ and $q(k)$. Among them, λ is the step parameter, which determines the update rate of the algorithm, θ is the phase, and T is the sampling time. In the adaptive algorithm, an update value is added to the adaptive parameters $p(k)$ and $q(k)$ according to the position error signal e. The performance of the AFC is determined by these values.

4.3.1 Single neuron PID

As to develop an accurate mathematical model, it is essential to achieve adaptive adjustment of control parameters to improve the dynamic performance of the control system. Three components, P (proportional), I (integral), and D (differential) are controlled based on fixed coefficients in a typical PID control, while single-neuron PID uses neural networks (or deep learning models) to automatically learn and adjust the weights of these components. Therefore, single neuron PID is more adaptive to environmental changes, which improves the effectiveness of control.

The neuron adaptive PID control algorithm is as follows:

$$u(k) = K_u\left\{W_1 e(k) + W_2 \sum_{j=0}^{k} e(j) + W_3\left[e(k) - e(k-1)\right]\right\} \tag{30}$$

where K_u is the adaptive coefficient. Both W_i and K_u can be adjusted online. W_i is modified according to the supervised delta learning rule:

Figure 5 AMEsim model of lifting system (see online version for colours)

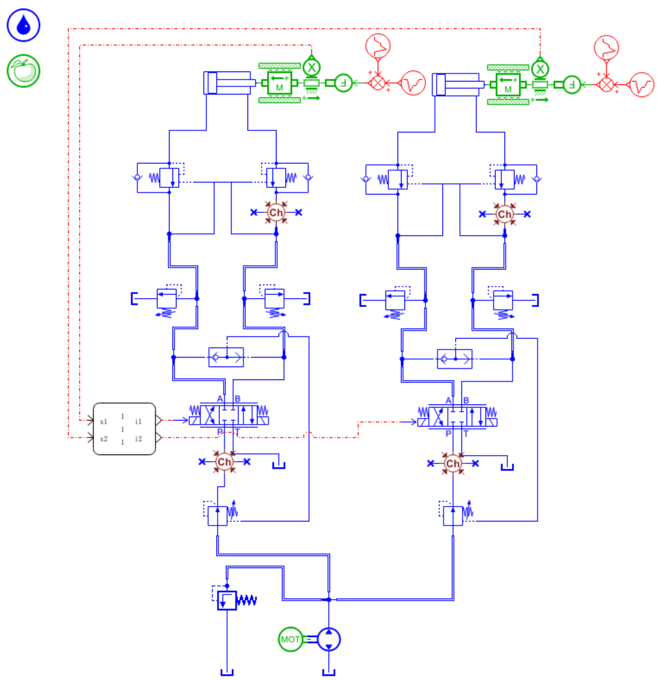

Table 1 Parameters of lifting system co-simulation model

Symbol	*Parameter*	*Value*	*Symbol*	*Parameter*	*Value*
q_s	Flow rate of the proportional valve	160 L/min	K_q	Flow gain	4L/(min·m A)
I	Input current	40 mA	V_e	Effective volume	0.0159 m^3
q_L	Flow rate of the lifting cylinder	320 L/min	C_{tp}	Total leakage coefficient	0.01
p_L	Load pressure of the lifting cylinder	33,000 N	βe	Oil volume elastic modulus	1,700 MPa
A_p	Non-rod chamber area of the lifting cylinder	132.665 cm^2	k	Area ratio between non-rod chamber and rod chamber	1.61
m	Mass of the segment	1,650 kg	B_p	Viscous damping coefficient	1,500 N/(m/s)
p_1	Rod chamber pressure	25 MPa	p_2	Non-rod chamber pressure	24.5MPa
F_L	Load interference force	9,000 N	A_0	Rod chamber area	82.425 cm^2
ξ	System damping coefficient	0.8	ω_k	System natural frequency	80 Hz
D	Piston diameter	130 mm	d	Rod diameter	80 mm
H	Cylinder stroke	1.2 m		Coulomb friction/static friction	4,000 N

$$\begin{aligned} W_i(k) &= W_i(k-1) + \eta_i \left[n_d(k) - n(k) \right] X_i(k) \\ K_u &= \eta_u \left| n_d(k) - n(k) \right| \end{aligned} \tag{31}$$

In the formula: η, η_u is the learning coefficient. It has a great impact on the anti-interference ability and adaptability of the entire control system.

5 Modelling and simulation verification

5.1 Hydraulic system AMESim model

AMESim hydraulic library is used to build the model of hydraulic components and hydraulic accessories to ensure the simulation efficiency. The hydraulic system is modelled using AMESim while the controller is designed using MATLAB/Simulink in Figure 5. The model parameters are shown in Table 1. Some parameters are identified by the actual system of the full-scale test bench. A hydraulic pump supplies oil to the independent hydraulic system of the left and right hydraulic cylinders respectively. Each set of hydraulic system mainly includes: hydraulic cylinder, balance valve, pressure reducing valve, relief valve, proportional reversing valve, pressure compensation valve, etc.

5.2 Signal pre-processing

The displacement signals of the lifting cylinder of the full-scale test bench were collected by the displacement sensor after the cylinder operated smoothly for a while under an unloaded condition. The pre-processing signal after removing the noise is shown in Figure 6. The signal-to-noise ratio has significantly reduced to –22.9364 db.

Figure 6 (a) Noise signal and (b) denoised signal (see online version for colours)

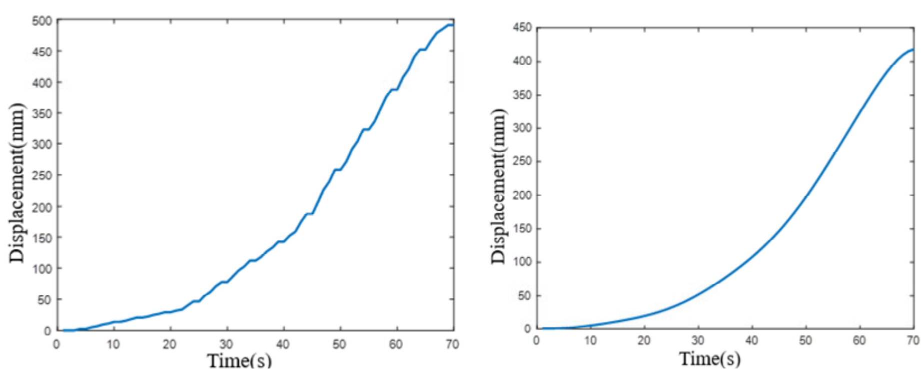

(a) (b)

5.3 Identification results

The comparison between the output curves identified by different methods and the actual output curves is shown in Figure 7.

Figure 7 Identification results of the displacement signals (a) output (top) and input (bottom) signals from the test rig (b) comparison between the least squares identification result of the forgetting factor and the actual displacement (c) comparison between the least squares identification result of the deviation compensation and the actual displacement (d) comparison between the identification result of this paper and the actual displacement (see online version for colours)

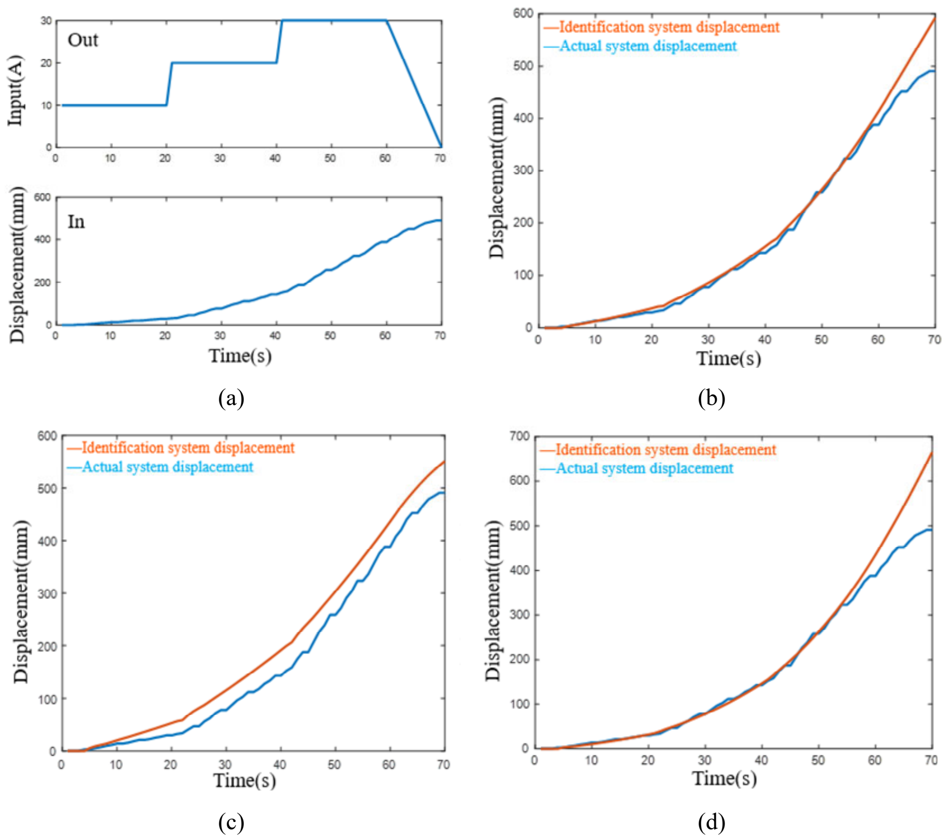

Figure 7 shows the identification results of the displacement signals using different methods. The parameter identified by the actual data of the test bench is a_0, a_1, a_2, B_1, B_2, B_3 of formula 19. The parameters identification results are shown in Table 2. The least squares identification result of the forgetting factor shows a noticeable deviation from 20 to 50 s, and 60 to 70 s while the least squares identification result of the deviation compensation indicates a quite large deviation over the whole range. Using the method presented in this paper shows a smaller deviation compared to the other two. The root mean square error (RMSE) values, indicated in Table 3, further show the identification method in this paper has a better effect on system modelling than other methods.

Table 2 Identification values of model parameters

Symbol	*Value*	*Symbol*	*Value*
a_0	0.3788	B_1	0.1995
a_1	0.276	B_2	0.1377
a_2	0.2343	B_3	0.17

Table 3 RMSE values of different identification methods

	(b)	*(c)*	*(d)*
RMSE	451.0735	413.2781	520.3336

5.4 *Tracking control simulation*

The different control effects of the proposed control method, SMC, and PID are verified by joint simulation. The parameters used in this control algorithm are left cylinder SMC: $c_1 = c_2 = 30$, $b = 1$, $a_1 = 4.343$, $a_2 = 1.232$, $k_0 = k_1 = 2.4$. Right cylinder SMC: $c_1 = c_2 = 30$, $b = 1$, $a_1 = 4.343$, $a_2 = 1.232$, $k_0 = k_1 = 2.9$. Adaptive feedforward cancellation: $\omega_d = 10$, $T = 0.1$, $\lambda = 1$. Single neuron PID: $k_p = 0.01$, $k_i = 0.01$, $k_d = 0$. In the simulation, the maximum speed of the left cylinder of the lifting cylinder is 100mm/s, and the maximum speed of the right cylinder is 80 mm/s. The operating speed of the left and right cylinders is 20 mm/s. The control period in Simulink is 0.01 s.

Figure 8 Control results using SMC, PID, and the proposed method of the left and the right cylinder displacement tracking and error curves (a) displacement tracking results of the left cylinde (b) displacement tracking results of the right cylinder (c) displacement tracking error of the left cylinder (d) displacement tracking error of the right cylinder (see online version for colours)

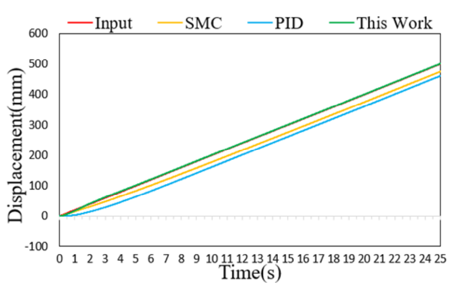

(a)

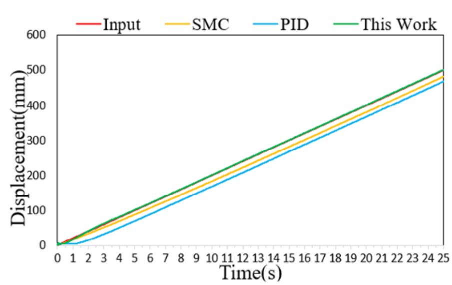

(b)

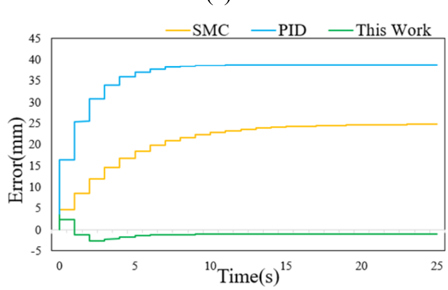

(c)

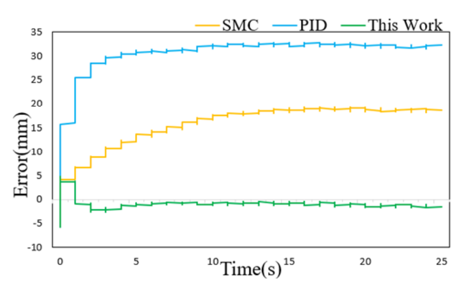

(d)

Figure 8 shows the displacement tracking and the tracking deviations of the left and the right cylinders. The steady-state error of the SMC method is 0.0247 m for the left cylinder and 0.0187 m for the right cylinder. The steady-state error of the PID method is 0.0387 m for the left cylinder and 0.0322 m for the right cylinder. The steady-state error of this method is 0.001 m for the left cylinder and 0.00148 m for the right cylinder, which are lower than those using the other two methods. From the tracking error curves, the system reaches a steady state in about 18 seconds under the PID control, in about 9 seconds under the SMC control, and in about 7 seconds using this proposed method. The results indicate that the proposed control method has quick responding and adjusting capability.

Figure 9 Synchronisation error between the left and the right cylinder using SMC, PID, and the proposed method (see online version for colours)

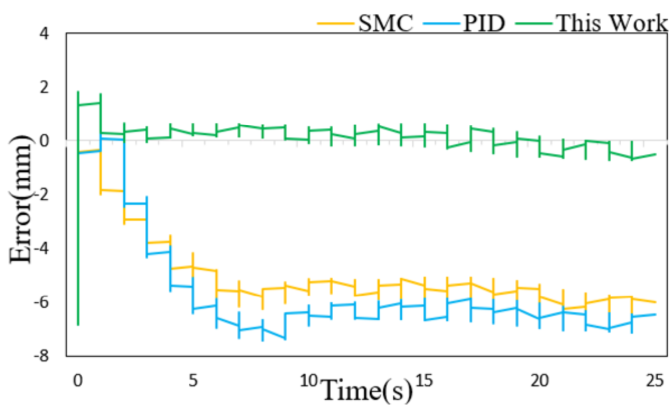

As can be seen from Figure 9, the synchronisation error of the SMC method is 5.99 mm. The synchronisation error of the PID method is 6.46 mm. The synchronisation error of the method in this chapter is 0.49 mm. The synchronisation error of this method is less than 1 mm.

6 Experiments

6.1 Description of the full-scale test bench

A customised full-scale test bench has been developed and shown in Figure 10. The test bench imitates the actual system and motion in a 6-metre TBM segment assembly procedure using actual concrete segments. The bench includes an assembling machine, a computer, a depth camera, an industrial computer, a Siemens S7-300 controller, an external pull-wire cylinder displacement sensor, and a rotary encoder. The system pressure of the test bench is 25 MPa, the system flow rate is 240 L/min, the motor power of the pumping station is 160 KW, and the control current of the reversing valve is 40 mA. The sampling period of the displacement sensor on the test bench is 0.1s. Some main parameters of the sensors and the test bench used are shown in the Tables 4 and 5 (Xiang et al., 2023a, 2023b). A complete process of automatic assembly includes (as shown in Figure 11):

1 a segment grasping step which is performed by a depth camera positioning and all relevant actuators

2 a segment transporting step that quickly transports a segment to a pre-defined position within the detective range of a depth camera based on translating, lifting, and rotating motions

3 a segment assembly which assembles the segment by performing fine tuning of pitch and swing motions based on the feedbacks from the depth camera.

Figure 10 Experimental bench for automatic segment assembly (see online version for colours)

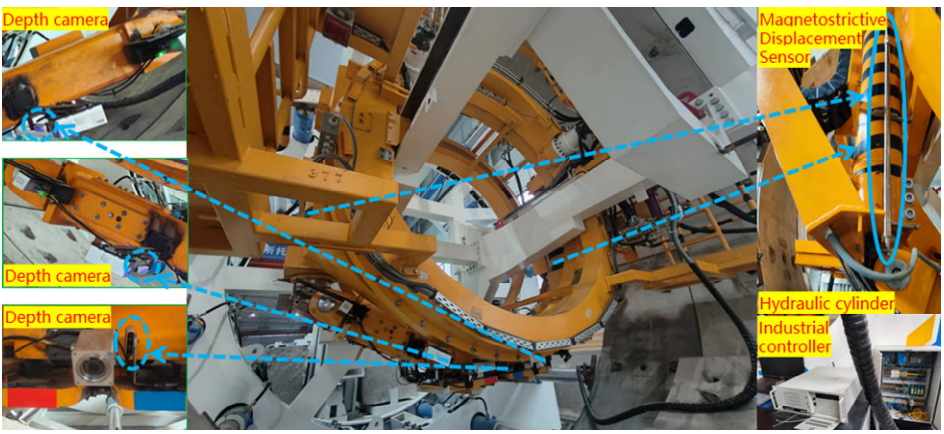

Table 4 Sensors used in the experiment and their parameters

Sensors	*Type*	*Main parameters*
Depth camera	Intel realsense D435i	RGB frame resolution: 1,920 × 1,080 depth accuracy: < 2%
		Depth output resolution:1,280 × 720 depth range: 0.1 m~10 m
Controller	Siemens S7-300	Bit memory: 8192 bit Processing time: < 0.01 us
Magnetostrictive displacement sensor	Tefophor	Measuring range: TH 25 mm~7,650 mm Linear accuracy:0.02%
Pull wire displacement sensor	Tefophor	Measuring range:0~1,000 mm linear accuracy: ±0.2%F.S.
Multiturn encoder	Ike	Maximum speed:6,000r/s accuracy: ±0.0439°

In the complete procedure, the success rate of the segment assembly is 83.33% in twelve assembly experiments using different types of segments. Automatic assembly of one piece of segment was performed within 3 min, which is significantly shorter than manual assembly. The misalignment in and between segment rings is less than 10 mm, which fulfills the requirement of segment assembly.

Table 5 Parameters of a full-size test bench for automatic segment erector

Assembly machine	*Parameter*	*Assembly machine*	*Parameter*
Rotary range	±220°	Segment outer diameter	6 m
Lifting distance	0.8~1.2 m	Translation velocity	Maximum speed 80 mm/s
Translation distance	1.2~2.1 m	Rotary distance	0~1.5 r/min
Fine angle (α, β, γ)	±2.5°	Lifting velocity	Maximum speed 13.3 mm/s

Figure 11 Assembly procedure in a full-scale test bench (see online version for colours)

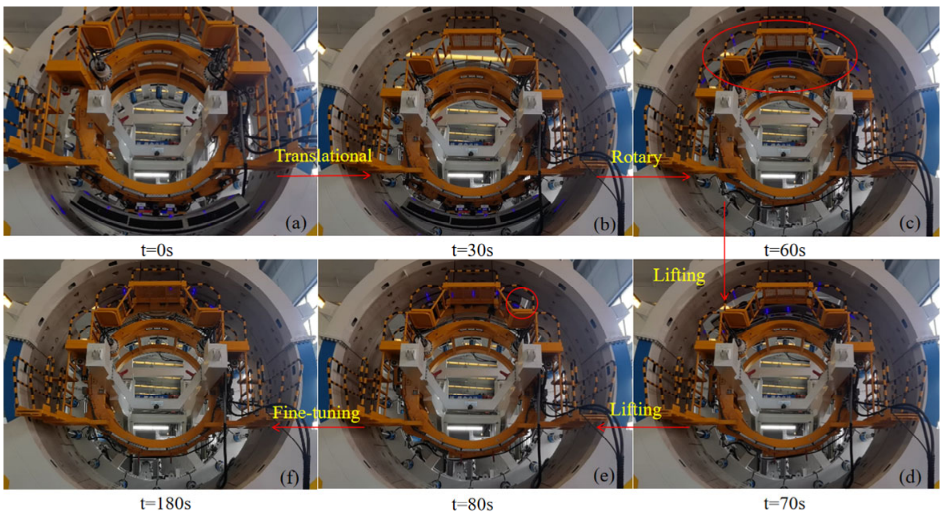

6.2 *Lifting cylinder in an independent movement*

Experiments of segment grasping were performed under an unloaded condition to simulate reality. Figure 12 shows the displacement tracking curves of the left and right cylinders using SMC, PID, and this method. The displacement tracking curves of the proposed method are closer to the input showing less hysteresis compared to those using SMC and PID. Figure 13 shows the displacement tracking errors using SMC, PID, and the proposed method. The operating speed of the left and right cylinders is 17 mm/s during the segment grabbing, i.e., no-load control. The steady-state error of the SMC method is 9.1 mm for the left cylinder and 18.68 mm for the right cylinder. The steady-state error of the PID method is 5.05 mm for the left cylinder and 11.67 mm for the right cylinder. The steady-state error of the proposed method is 1.96 mm for the left cylinder and 3.59 mm for the right cylinder, which are significantly lower than those using the other two methods.

Figure 14 shows the synchronisation error of the SMC method is 9.58 mm and 6.62 mm using PID. The synchronisation error of this method is 1.63 mm which is much lower than the other two methods indicating the proposed method has a better synchronisation in segment grasping.

Figure 12 Displacement tracking results of different control methods for (a) left cylinder and (b) right cylinder under an unloaded condition (see online version for colours)

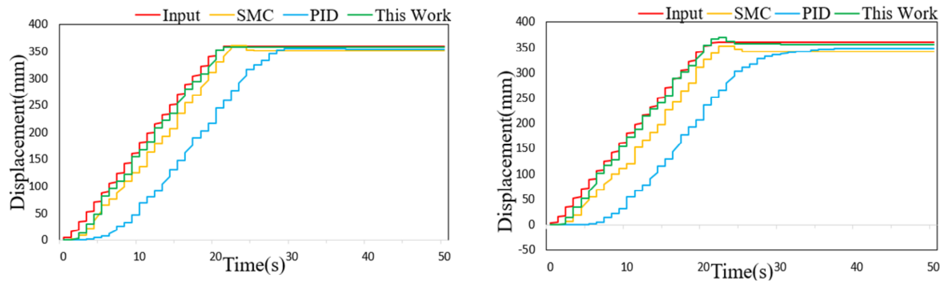

(a) (b)

Figure 13 Displacement tracking error of different control methods for (a) left and (b) right cylinder (see online version for colours)

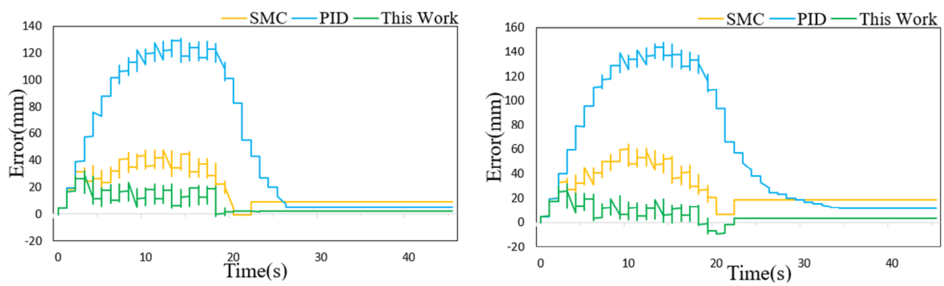

(a) (b)

Figure 14 Synchronisation error of left and right cylinders (see online version for colours)

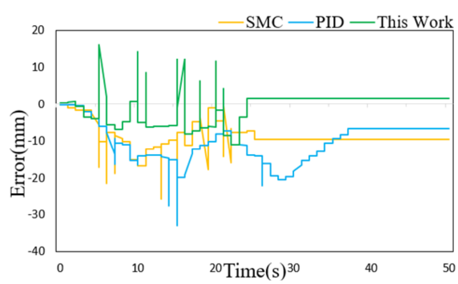

To verify the control effect during assembly, the lifting control experiment was carried out using a standard segment weighing approximately 3.3 tons. The operating speed of the left and right cylinders is 7 mm/s during the segment rough assembly, i.e., load control. Figure 15 shows the displacement tracking curves of the left and right cylinders. By controlling the lifting motion under a loaded condition, the difference between the curves obtained using the proposed method and the actual measurement is slightly larger than those under an unloaded condition indicating a large load may mildly affect the two-cylinder synchronisation. On the other hand, the proposed method still has less hysteresis than the SMC and PID methods. Moreover, the system reaches a steady state in approximately 26 seconds using PID, 21 seconds under SMC, and only 19 seconds using the proposed method. This shows that the proposed method performs in a quick response and adjusting manner under a loaded condition.

Figure 15 Displacement tracking results of different control methods for (a) left cylinder and (b) right cylinder in loaded conditions (see online version for colours)

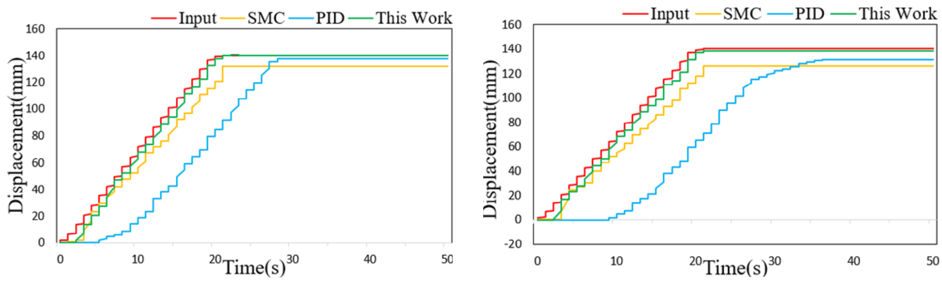

(a) (b)

Figure 16 Displacement tracking error of different control methods for (a) left cylinder and (b) right cylinder in loaded conditions (see online version for colours)

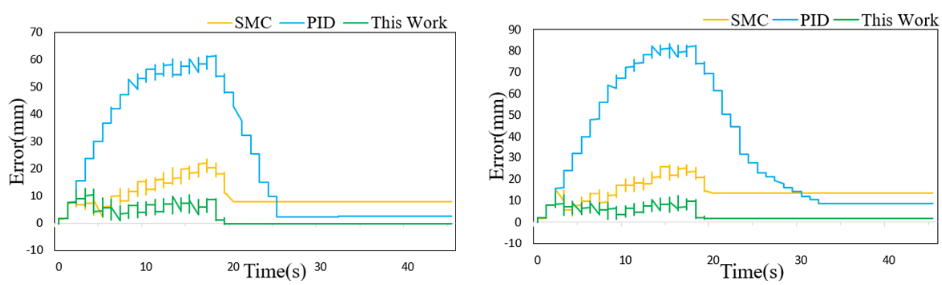

(a) (b)

Figure 16 shows the displacement tracking error of the left and right cylinders. The steady-state error of SMC is 7.89 mm for the left cylinder and 13.67 mm for the right cylinder. The steady-state error of PID is 2.5 mm for the left cylinder and 8.68 mm for the right cylinder. The steady-state error of the proposed method is 0.23 mm for the left cylinder and 1.66 mm for the right cylinder. Compared with the results obtained under an unloaded condition, the hysteresis time of the loaded lifting cylinder is significantly increased since large loads increase inertia forces leading to a noticeable overshoot. However, the maximum error and overshoot are reduced under a loaded condition compared to those under an unloaded condition, which may be because the difference between the gravity and friction between the cylinder and the load decreases under the loaded condition. From the comparison between Figure 8 and Figure 16, it can be seen that the simulation error gradually increases while the experimental error first increases and then decreases, which is related to the hysteresis of the actual system.

Figure 17 indicates that the synchronisation error of this method is smallest, approximately 2 mm, compared to those using SMC (5.78 mm) and PID (6.18 mm). From the comparison between Figure 9 and Figure 17, it can be seen that the synchronisation error curve in the simulation is relatively stable, but the experimental synchronisation error curve has a large vibration, a large curve peak, and a large maximum error. This is related to system hysteresis and vibration.

Figure 17 Synchronisation error of left and right cylinders (see online version for colours)

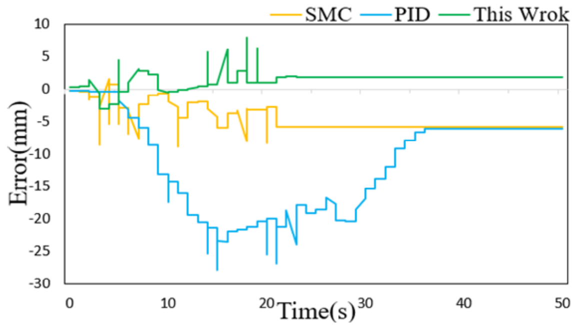

The control algorithm designed in this paper takes into account the response speed, control accuracy and synchronisation. It has a good inhibitory effect on the hysteresis and nonlinearity of the hydraulic system, but the dead zone problem cannot be solved by the control method in this paper. At the same time, the control accuracy needs to be further improved.

6.3 Lifting cylinder in a compound motion

In actual segment assembly, compound motion is commonly used since it saves time. Herein, the compound motion of translating-lifting was conducted to verify the complete procedure. The control method in this paper is also adopted for the lifting motion, and PID control is adopted for the translating motion. The lifting displacement is 0 to 140 mm while the translating displacement is 0 to 360 mm.

Figure 18 Compound motion tracking displacement (a) tracking error (b) and synchronisation error (b) curves of the left and right cylinders (see online version for colours)

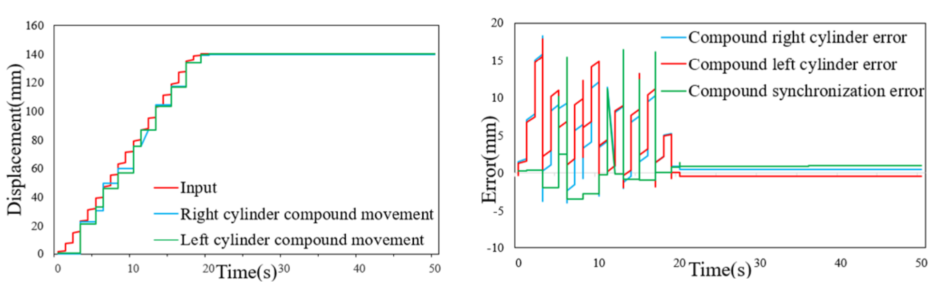

(a) (b)

In segment grasping, the compound experiment was performed under an unloaded and large-stroke condition. Figure 18(a) shows the tracking displacement curves of the left and right lifting cylinders in the compound motion. It can be seen that the impact of the compound motion on the lifting motion of the left and the right cylinders is the same as those in independent motions. The synchronisation of the left and the right cylinders is acceptable in the compound motion.

Figure 18(b) shows the steady-state error and synchronisation error curves of the left and right cylinders during compound motion. The steady-state error of the left cylinder is 0.517 mm, while the steady-state error of the right cylinder is –0.452 mm. The synchronisation error is 0.97 mm. The results indicate that the synchronisation of the left and right cylinders is better and the steady-state error is smaller in the compound motion compared to those in independent motions.

Figure 19 Displacement tracking curves of the (a) left and the (b) right cylinders in translating-lifting compound motion compared to independent lifting motion (see online version for colours)

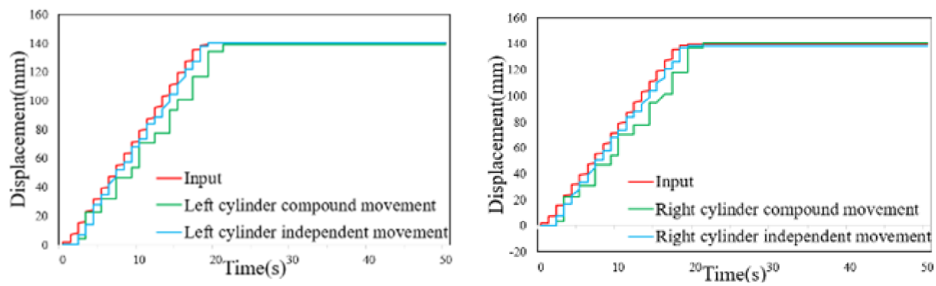

(a) (b)

Figure 20 Displacement tracking error curves of (a) the left and (b) the right cylinders in the translating-lifting component and independent lifting motions (see online version for colours)

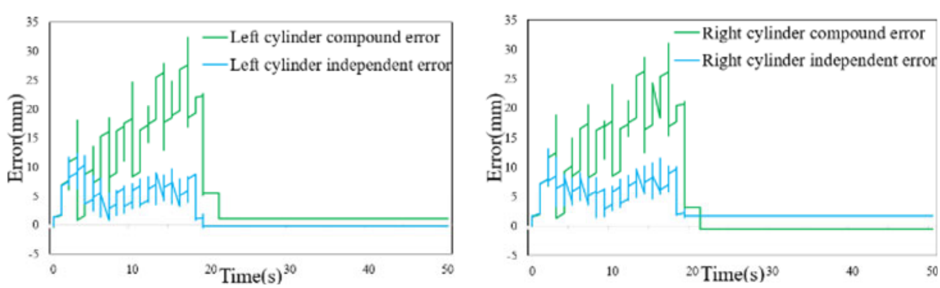

(a) (b)

In the segment transporting step, the translating-lifting motion experiments were performed under a loaded and large-stroke condition. Figure 19 shows the displacement tracking curves of the right and left cylinders in the compound motion and the independent motion. In the figure, red is the expected tracking displacement, blue is the independent motion displacement, and green is the composite motion displacement. Figure 20 shows the tracking errors of the left and the right cylinders in the translating-lifting compound motion and the independent lifting motion. The steady-state error of the compound motion of the right cylinder is –0.629 mm, and that of the left cylinder is 1.09 mm, compared to 1.66 mm in the independent motion of the right cylinder and –0.23 mm in the independent motion of the left cylinder. The error is still below 2 mm though the vibration of the compound motion is larger than that of independent motion.

It is found that the hysteresis time and maximum error of the lifting cylinder in the loaded compound motion are significantly larger than those in the unloaded compound motion due to load-induced vibration and deformation in the system. Moreover, the hysteresis time and maximum error are also much larger in the compound motion than those in the independent motion. This is because the flow rate and the pressure of the supplied hydraulic oil to the system reduce in the compound motion. Moreover, large vibration was also experienced during the compound motion compared to the independent motion.

Figure 21 Synchronous tracking error of the left and right cylinders in the compound and independent motion (see online version for colours)

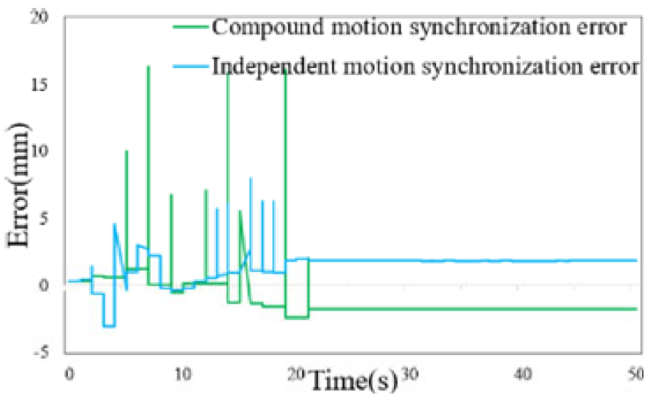

Figure 21 shows the synchronous tracking errors of the left and right cylinders in the compound and independent motions. The synchronous error of the compound motion between the left and right cylinders is –1.72 mm while that of the independent motion is 1.89 mm due to the increased vibration in the compound motion. However, the synchronisation error is still below 2 mm which fulfills the system requirement.

7 Conclusions

This paper presents a comprehensive procedure to develop a control method to achieve automation and synchronisation of the electro-hydraulic lifting system in tunnel boring segment assembly. The paper enables the following conclusions to be drawn:

- Due to heavy and uneven loading, large vibration, uncertainty of parameters, and nonlinear friction, an identification algorithm based on the improved deviation compensation recursive least squares with forgetting factor was used instead of developing a complete physical model, which was verified to be a practical measure to be used in a high complicated engineering system.
- SMC with improved sliding mode approach rate and the deviation coupling method of fusion single neuron PID were designed and the simulation results indicated that the proposed method had a good performance compared to those using SMC, PID.

- Experimental results conducted on a full-scale test bench provided strong evidence that the proposed method could fulfil the engineering requirements in the independent and compound motion under both loaded and unloaded conditions.

Declarations

This work is supported by the National Key Research and Development Program of China (Grant No. 2022YFB4602502), the National Natural Science Foundation of China (Grant No. 52222503), the Natural Science Foundation of Zhejiang Province (Grant No. LD22E050003).

One of the authors of this paper is an editorial board member for this journal.

References

Chen, C.S. and Hu, N.T. (2022) 'Model Reference adaptive control and fuzzy neural network synchronous motion compensator for gantry robots', *Energies*, January, Vol. 15, No. 1, p.17.

Chen, X., Wang, Y., Cai, L.T.J., Liu, F., Yang, H. and Zhu, Y. (2023) 'Autonomous recognition and positioning of shield segments based on red, green, blue and depth information', *Automation in Construction*, February, Vol. 146, p.11.

Ding, H.G., Li, Y.L., Zhu, Q.M. and Su, J.Y. (2024) 'Position servo with variable speed pump-controlled cylinder: design, modelling and experimental investigation', *International Journal of Hydromechatronics*, Vol. 7, No. 2, p.22.

Guo, Q., Li, X.C., Zuo, Z.Y., Shi, Y. and Jiang, D. (2021) 'Quasi-synchronization control of multiple electrohydraulic actuators with load disturbance and uncertain parameters', *IEEE-Asme Transactions on Mechatronics*, August, Vol. 26, No. 4, pp.2048–2058.

Guo, Y.N., Zhang, Z., Liu, Q.Y., Nie, Z. and Gong, D.W. (2022) 'Decoupling-based adaptive sliding-mode synchro-position control for a dual-cylinder driven hydraulic support with different pipelines', *ISA Transactions*, April, Vol. 123, pp.357–371.

Han, H.Y., Liu, Y., Ma, L.F., Liu, Z.Q. and Quan, L. (2018) 'Analyze the characteristics of electro-hydraulic servo system's position-pressure master-slave control', *Advances in Mechanical Engineering*, June, Vol. 10, No. 6, p.9.

Hao, Z.Y., Li, X., Cao, X., Gan, Y., Yu, Q. and Zhang, Q.Y. (2020) 'A cross-coupled control strategy of phase difference for electric vibration damping actuator', *IEEE Access*, Vol. 8, pp.213887–213898.

Hu, K. and Zhang, W.Y. (2022) 'Position control algorithm of fuzzy adaptive PID of hydraulic interconnected suspension under load impact disturbance', *IEEE Access*, Vol. 10, pp.39665–39673.

Kroll, A. and Fischer, J. (2021) 'On approximate maximum likelihood estimation of dynamic Takagi-Sugeno multi-models: method and application to a servo-pneumatic drive', *At-Automatisierungstechnik*, October, Vol. 69, No. 10, pp.858–869.

Kuang, Z.A., Gao, H.J. and Tomizuka, M. (2021) 'Precise linear-motor synchronization control via cross-coupled second-order discrete-time fractional-order sliding mode', *IEEE-Asme Transactions on Mechatronics*, February, Vol. 26, No. 1, pp.358–368.

Li, G.Q., Ding, Y.T., Feng, Y. and Li, Y.S. (2019) 'AMESim simulation and energy control of hydraulic control system for direct drive electro-hydraulic servo die forging hammer', *International Journal of Hydromechatronics*, Vol. 2, No. 3, pp.203–225.

Li, L., Cheung, N., Yang, G.L., Wang, C.C., Fu, P.F., Li, G.C. and Pan, J.F. (2022) 'Design of a variable-gain adjacent cross-coupled controller for coordinated motion of multiple permanent magnet linear synchronous motors', *Computers and Electronics in Agriculture*, January, Vol. 192, p.13.

Li, Q., Fang, Y.M., Li, J.X. and Zhang, W.J. (2020) 'Feedforward and feedback compound control of vibration displacement for a continuous casting mold driven by a servo motor', *International Journal of Control Automation and Systems*, December, Vol. 18, No. 12, pp.3218–3228.

Li, S. and Cao, X.H. (2021) 'Synchronous control characteristics analysis of shield propulsion hydraulic system based on tracking differentiator and self-adaptive nonlinear PID', *International Journal of Pattern Recognition and Artificial Intelligence*, November, Vol. 35, No. 14, p.18.

Li, X., Zhou, W.L., Jia, D., Qian, J.Z., Luo, J., Jiang, P. and Ma, W.L. (2022) 'A decoupling synchronous control method of two motor or large optical telescope', *IEEE Transactions on Industrial Electronics*, December, Vol. 69, No. 12, pp.13405–13416.

Lin, J.J., Song, J. and Lu, C. (2022) 'Synchrophasor data analytics: transmission line parameters online estimation for energy management', *IEEE Transactions on Engineering Management*, June, Vol. 69, No. 3, pp.671–681.

Liu, T., Gong, G.F., Yang, H.Y., Chen, Y.X. and Zhu, Y. (2019) 'Trajectory control of tunnel boring machine based on adaptive rectification trajectory planning and multi-cylinders coordinated control', *International Journal of Precision Engineering and Manufacturing*, October, Vol. 20, No. 10, pp.1721–1733.

Liu, Z.T., Lin, W.Y., Yu, X.H., Rodriguez-Andina, J.J. and Gao, H.J. (2022) 'Approximation-free robust synchronization control for dual-linear-motors-driven systems with uncertainties and disturbances', *IEEE Transactions on Industrial Electronics*, October, Vol. 69, No. 10, pp.10500–10509.

Ma, T.B., Guo, X.X., Su, G.Y., Deng, H.S. and Yang, T. (2023) 'Research on synchronous control of active disturbance rejection position of multiple hydraulic cylinders of digging-anchor-support robot', *Sensors*, April, Vol. 23, No. 8, p.32.

Qi, J., Guo, Q., Ren, H.L., Chen, Z.L., Yan, Y. and Jiang, D. (2022) 'Control synchronization design of a multiple electrohydraulic actuator system with linearization dynamics and an external disturbance observer', *Electronics*, December, Vol. 11, No. 23, p.16.

Qian, P.F., Liu, L., Pu, C.W., Meng, D.Y. and Páez, L.M.R. (2023) 'Methods to improve motion servo control accuracy of pneumatic cylinders-review and prospect', *International Journal of Hydromechatronics*, Vol. 6, No. 3, p.8.

Shi, P.W., Sun, W.C., Yang, X.B., Rudas, I.J. and Gao, H.J. (2023) 'Master-slave synchronous control of dual-drive gantry stage with cogging force compensation', *IEEE Transactions on Systems Man Cybernetics-Systems*, January, Vol. 53, No. 1, pp.216–225.

Sun, C.G. and Yuan, R.B. (2021) 'Adaptive robust cross-coupling position synchronization control of a hydraulic press slider-leveling', *Science Progress*, January, Vol. 104, No. 1, pp.1–19.

Wang, B.F., Iwasaki, M. and Yu, J.P. (2022) 'Command filtered adaptive backstepping control for dual-motor servo systems with torque disturbance and uncertainties', *IEEE Transactions on Industrial Electronics*, February,Vol. 69, No. 2, pp.1773–1781.

Wang, Y., Zhao, J., Man, J. and Ding, H. (2022) 'Multi-cylinder synchronization control strategy with state constraint based on disturbance observer', *Journal of South China University of Technology*, Natural Science Edition, Vol. 50, No. 2, p.93.

Wu, W.Q., Gong, G.F., Huan, Q., Zhou, X.H., Chen, Y.X. and Peng, X.B. (2022) 'Investigation into the electrohydraulic synchronous motion control of a thrust system for a tunnel boring machine', *Machines*, February, Vol. 10, No. 2, p.17.

Xiang, P., Yan, L., Guo, Y., He, X., Gerada, C. and Chen, I-M. (2023a) 'A concentrated-flux-type pm machine with irregular magnets and iron poles', in *IEEE/ASME Transactions on Mechatronics*, Vol. 29, No. 1, pp.691–702.

Xiang, P., Yan, L., Xiao, H., He, X. and Du, N. (2023b) 'Development of a novel radial-flux machine with enhanced torque profile employing quasi-cylindrical PM pattern', in *IEEE Transactions on Energy Conversion*, Vol. 38, No. 4, pp.2772–2783.

Yabui, S. and Inoue, T. (2019) 'Development of adaptive feed-forward cancellation with frequency estimation algorithm for compensation of periodic disturbance at arbitrary frequency', *Journal of Dynamic Systems Measurement and Control-Transactions of the ASME*, December, Vol. 141, No. 12, p.12.

Yang, H.Y., Shi, H. and Gong, G.F. (2010) 'Motion control of thrust system for shield tunneling machine', *Journal of Central South University of Technology*, June, Vol. 17, No. 3, pp.537–543.

Yuan, H. and Zhao, X.M. (2022) 'Advanced contouring compensation approach via Newton-ILC and adaptive jerk control for biaxial motion system', *IEEE Transactions on Industrial Electronics*, May, Vol. 69, No. 5, pp.5081–5090.

Yuan, M., Manzie, C., Good, M., Shames, I., Gan, L., Keynejad, F. and Robinette, T. (2020) 'A review of industrial tracking control algorithms', *Control Engineering Practice*, September, Vol. 102, p.3.

Zerdali, E., Yildiz, R., Inan, R., Demir, R. and Barut, M. (2021) 'Improved speed and load torque estimations with adaptive fading extended Kalman filter', *International Transactions on Electrical Energy Systems*, January, Vol. 31, No. 1, p.16.